

APPLICATIONS OF PHASE DIAGRAMS TO STEEL PROCESSING

Tooru Matsumiya¹

Abstract

Examples of the application of CALPHAD method to steel processing are discussed. First, a complete stepwise simulation of solidification microsegregation is shown, both with and without back diffusion. Second, solidification of weld pool of Fe-Cr-Ni alloys is simulated using a special method for combining of solute diffusion analysis. Then, a coupled precipitation model is discussed for the estimation of chemical compositions change of nonmetallic inclusions during solidification of steel focusing in HIC resisting steels. Additionally, applications of a coupled reaction model based on local equilibrium calculation at slag-metal interface is presented and its use is demonstrated in the optimization of manganese removal process and in mold powder composition design. Finally, two examples of process condition design to obtain optimized properties are presented. One for controlling the amount and hardness of martensite in thick plates of 0.12%C-steel. Another for determining the solution temperature to obtain uniform and fine distribution of carbides and nitrides. Conditions for anti-erosion properties of bearing steel are also achieved by proper distribution of carbides using an estimation by the CALPHAD method.

Keywords: CALPHAD; Solidification; Microsegregation; Nonmetallic inclusion; Refining; Mold flux; Quenching; Solution treatment.

A APLICAÇÃO DE DIAGRAMAS DE FASES AO PROCESSAMENTO DE AÇOS

Resumo

Exemplos da aplicação do método CALPHAD no processamento de aços são discutidos. Inicialmente, uma simulação passo-a-passo da microsegregação é apresentada, considerando ou não a redistribuição de soluto no sólido. O segundo exemplo apresenta a simulação da poça de solda de ligas Fe-Cr-Ni usando um método especial para combinar a análise da difusão dos solutos. Um modelo de precipitação acoplado é discutido a seguir, para a estimativa das mudanças de composição das inclusões não-metálicas durante a solidificação do aço, como foco em aço resistente a HIC. Adicionalmente, aplicações de um modelo de reações acopladas para o cálculo do equilíbrio local nas interfaces metal-escória é apresentado e seu uso demonstrado na otimização da remoção do manganês e no projeto de pós de cobertura de lingotamento. Por fim, dois exemplos de otimização das condições de processamento são apresentados. Um, para controlar a quantidade e dureza da martensita em chapas grossas de 0,12% de C. Outro, discutindo as condições ideais do tratamento de solubilização para obter uma dispersão ideal de carbonetos e nitretos para o processamento e propriedades do aço. O controle das propriedades de erosão em aços para rolamentos é também demonstrado pela otimização da distribuição destes, via o método CALPHAD.

Palavras-chave: CALPHAD; Solidificação; Microsegregação; Inclusões não-metálicas; Tempera; Solubilização; Pó fluxante.

1 INTRODUCTION

CALPHAD stands for CALculation of PHase Diagrams, where Gibbs free energy of phases are assessed as functions of compositions of phases, temperature and pressure so that the phase diagrams obtained by thermodynamic equilibrium calculations among phases using the assessed Gibbs free

energy values agree with experimentally measured phase diagrams. By the use of these assessed Gibbs free energy functions of various phases, thermodynamic equilibrium relations, which appear in steelmaking processes at reaction interfaces, can also be analyzed. With the combination of the

¹ Graduate School of Natural Science & Technology, Kanazawa University, Kanazawa. Osaka Electro-Communication University, Neyagawa. Science Council of Japan; The Japan Society for Industrial and Applied Mathematics, Shinbashi, Minato-ku; Formerly, Nippon Steel Corporation, Chiyoda, Tokyo, Japan. E-mail: matsumiya.tooru@gmail.com



analysis of macroscopic transport and the equilibria analyses at reaction interfaces, various steelmaking processes are simulated for its optimization. In this paper, examples of this technique are shown as well as direct use of phase diagram calculation to predict existing phases during steelmaking processes for the optimization.

2 SOLIDIFICATION PATH ANALYSIS

2.1 Analysis of Solidification Microsegregation [1]

Solidification microsegregation can be expressed by the derivative forms of Clyne-Kurz's equation [2], Equation 1, and Scheil's equation [3], Equation 2:

$$(1-k^i)C_L^i df_s = \{1 - (1-2\Omega^i k^i) f_s\} dC_{L(C-K)} \quad (1)$$

$$(1-k^i)C_L^i df_s = \{1 - f_s\} dC_{L(Scheil)} \quad (2)$$

Where C_L^i : the concentration of solute i in residual liquid; $dC_{L(C-K)}$ and $dC_{L(Scheil)}$: increment of solute concentration in the residual liquid during the increment of solid fraction df_s according to Clyne-Kurz's equation and Scheil's equation, respectively; k^i : liquid-solid equilibrium partition coefficient of solute i ; f_s : fraction of solid and Ω^i : solidification parameter modified by Clyne-Kurz. In Scheil's equation, where back diffusion of solute into the solid phase is neglected, solute rejected at the solid-liquid interface due to the solid fraction increment all goes into liquid phase with the fraction $(1 - f_s)$ and increases its concentration. On the other hand, in the Clyne-Kurz's equation, some of the solute rejected at the solid-liquid interface goes into solid phase by back diffusion, $2\Omega^i k^i f_s dC_L$, and the rest goes in to liquid phase. By comparison between the two equations the relation between increments of solute i concentration calculated by Clyne-Kurz's equation and Scheil's equation, respectively, is derived as follows:

$$dC_{L(C-K)} = \{1 - f_s\} dC_{L(Scheil)} / \{1 - (1 - 2\Omega^i k^i) f_s\} \quad (3)$$

Solidification microsegregation by Equation 2 can be calculated stepwise as follows: the temperature of a system with solute concentration C_0 is decreased from its liquidus temperature a little bit and the thermodynamic equilibrium calculation at this temperature gives the amount of solid precipitation and solute concentrations in solid phase and liquid phase. Then, the precipitated solid phase is discarded out of the system and the temperature of the residual liquid is decreased a little bit again. The thermodynamic equilibrium calculation of the system at the lowered temperature gives newly precipitated solid fraction and solute concentration of the solid and residual liquid phases.

Then the newly precipitated solid phase is discarded out of the system again. By the repetition of these procedures, solidification microsegregation by Scheil's equation is calculated stepwise. The difference in solute concentration

of the residual liquid and amount of newly precipitated solid phase between two adjacent steps correspond to $dC_{L(Scheil)}$ and df_s , respectively.

By inserting the procedure that the solute increment between two adjacent steps is modified from $dC_{L(Scheil)}$ to $dC_{L(C-K)}$ by the use of Equation 3, solidification microsegregation by Equation 1 can be realized. That is, the solute concentration in the residual liquid is reset by the addition of $dC_{L(C-K)}$ to the solute concentration in the liquid at the previous step.

Simulated microsegregation calculations in Fe-21%Cr-11%Ni alloy are compared in Figure 1. Liquidus temperature of residual liquid calculated based on equilibrium solidification is the highest, that based on Scheil's equation, no diffusion in solid, is the lowest and that based on Clyne-Kurz's equation is in between, corresponding to the order of severity of simulated segregation.

2.2 Solidification Microstructure of Fe-Ni-Cr Alloy [4]

Dendrite shape is modeled as shown in Figure 2a. Solute diffusion along primary dendrite axis is neglected and diffusion in radial direction in its transverse cross section is analyzed in combination with the phase transformation. Considering the symmetry of diffusion, the triangle section is chosen for the analysis and sectioned into finite segments along the radial direction, as shown in Figure 2b. Solute diffusion is calculated between adjacent segments in every time step by finite difference method and solute concentration in each segment is updated. Local thermodynamic equilibrium is calculated in every segment for each time step by using updated solute concentrations. Complete mixing of solute is assumed in liquid phase. From the location of the segment

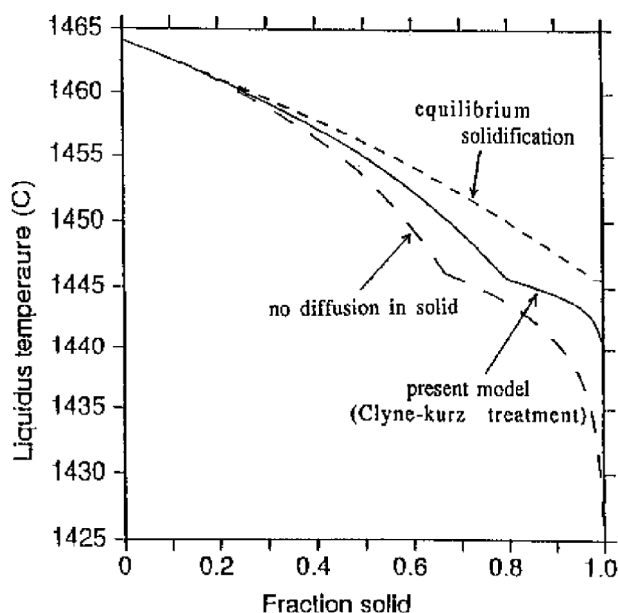


Figure 1. Liquidus temperature of the residual liquid with solute concentration calculated by various solidification microsegregation model as functions of fraction solid [1].

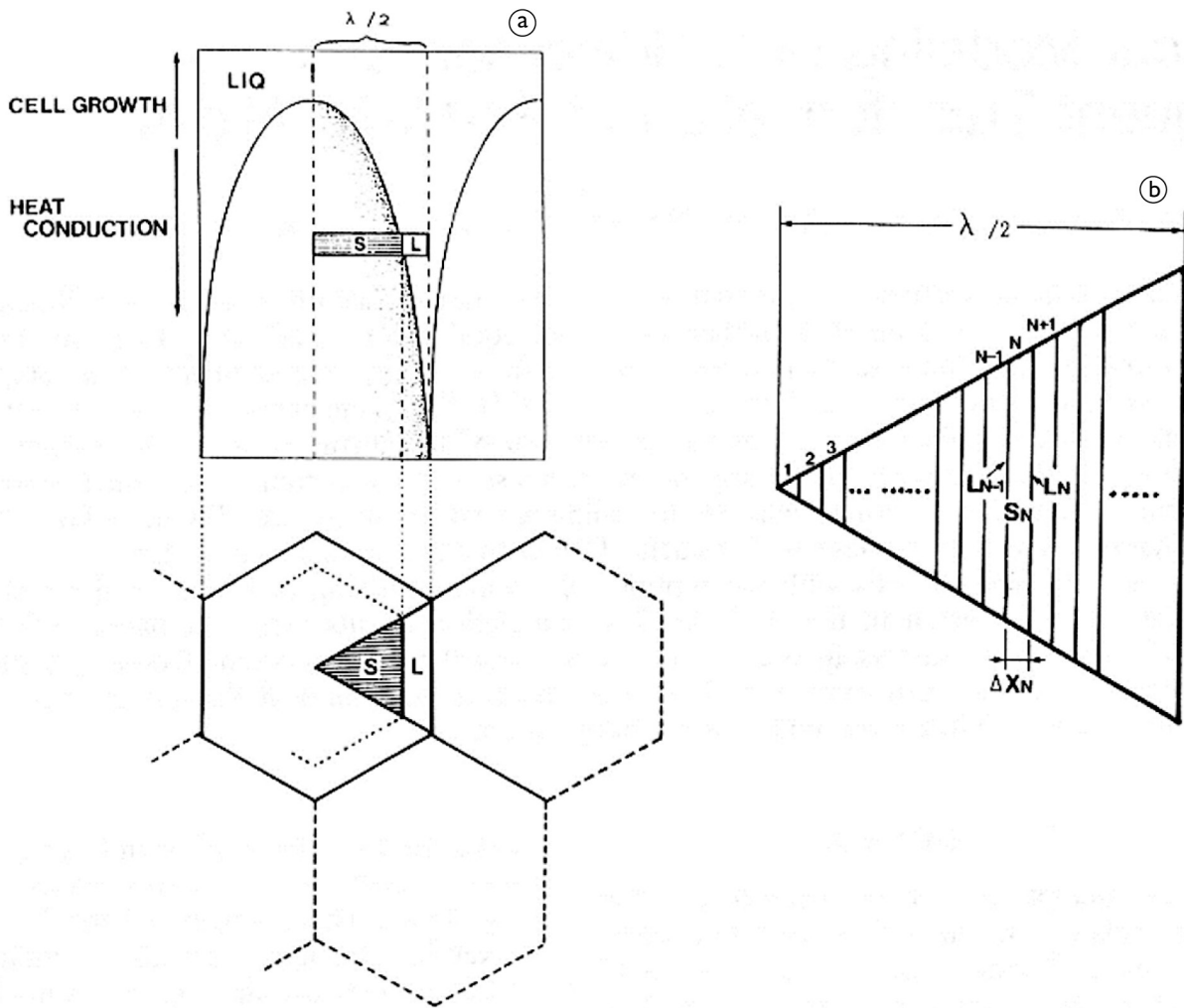


Figure 2. Cross-sections of modeled dendrite (a) and analyzed region chosen from the transverse cross-section (b) [4].

where both the solid and liquid phases coexist and their fractions, the location of solid-liquid interface along the radial direction is determined. Complete mixing of solute in delta solid phase is also assumed in each segment and solute diffusion between segments are analyzed only through delta solid phase. Since the diffusion of solute is much slower in gamma phase, solute diffusion between segments through gamma phase is neglected. Back diffusion of solutes into gamma phase during delta to gamma transformation in each segment is considered and the delta to gamma transformation is analyzed similar to the solidification based on Clyne-Kurz type segregation equation, since complete mixing of solute in delta phase in each segment is assumed.

Figure 3 shows the simulated results for welding pool solidification of Fe-18%-12%Ni alloy. During the first 0.7 s only gamma phase, primary solid, precipitates and its fraction increases as time elapses and afterwards delta phase also precipitates. At approximate 1.0 s solidification is completed. Delta fraction reaches 4% at this moment and decreases to 1% at the time of 2.5 s due to delta to

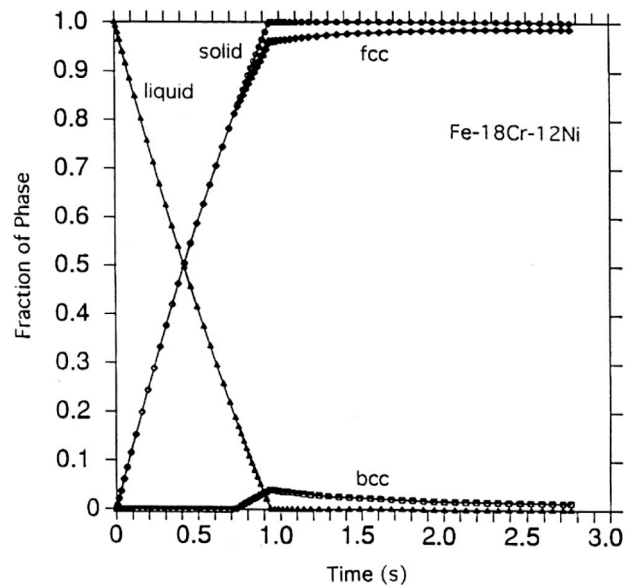


Figure 3. Calculated fractions of various phases in the weld pool of Fe-18Cr-12Ni alloy as time elapses [4].

gamma transformation, when the temperature is below 800K, transformation does not proceed any more. That is, the residual delta phase fraction of this alloy is 1% under the welding condition. Solidification of weld pool of various Fe-Cr-Ni alloys were simulated and calculated ratios of residual delta ferrite are compared with experimentally obtained values in Figure 4. Although the simulated results of primary solid phase are different from the observed one and the calculated delta fraction are little bit smaller than measured ones in some cases, the agreement between simulation and observation is not so bad. By this simulation alloy composition and welding parameter can be adjusted so that the desired amount of residual ferrite is obtained which affects welding cracking.

3 CONTROL OF NONMETALLIC INCLUSIONS

3.1 Coupled Precipitation Model [5]

Solidification microsegregation is analyzed with consideration of back diffusion into the solid phase and the nonmetallic inclusions are assumed to be in thermodynamic equilibrium with the residual liquid and trapped by solid phase as solidification proceeds without being pushed out from solid-liquid interface in coupled precipitation model as shown in Figure 5. The flow chart of the stepwise calculation of the coupled precipitation model is indicated in Figure 6.

At the beginning the system temperature is lowered little by little and the liquidus temperature is found. Next the temperature is lowered from the melting temperature so that the thermodynamic equilibrium calculation at this temperature gives the solid fraction with a predetermined

value, such as 0.01, by adjusting system temperature. When the temperature is determined, thermodynamic equilibrium is calculated to provide the solute concentrations of liquid and solid phases and the amount and compositions of nonmetallic inclusions. The increment of solute concentration in liquid phase is modified from the increment based on Scheil's equation to that based on Clyne-Kurz's equation as mentioned in section 2.1 and the soluble solute concentration in the residual liquid is revised with the consideration of solute back diffusion. The portion of nonmetallic inclusions which is left in the residual liquid phase is added to soluble solutes and total solute concentrations in residual liquid are obtained. The temperature of the liquid phase with this total

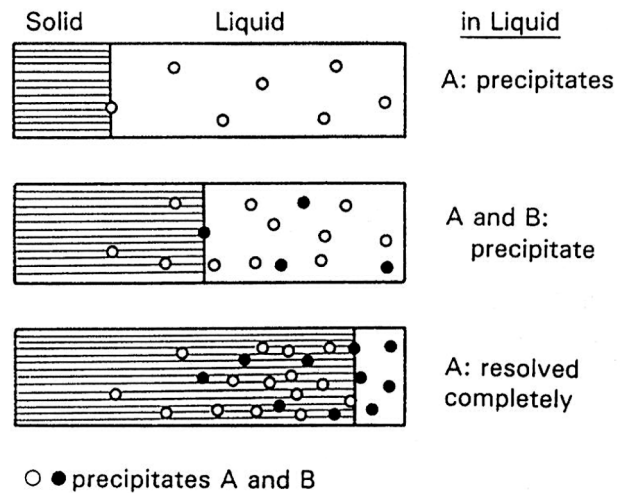


Figure 5. Schematic view of coupled precipitation model [5].

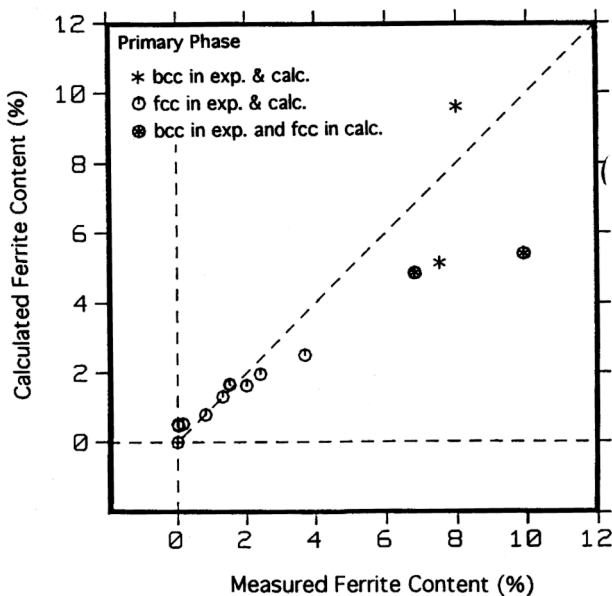


Figure 4. Comparison between calculated and measured fractions of residual delta ferrite for various Fe-Cr-Ni alloys [4].

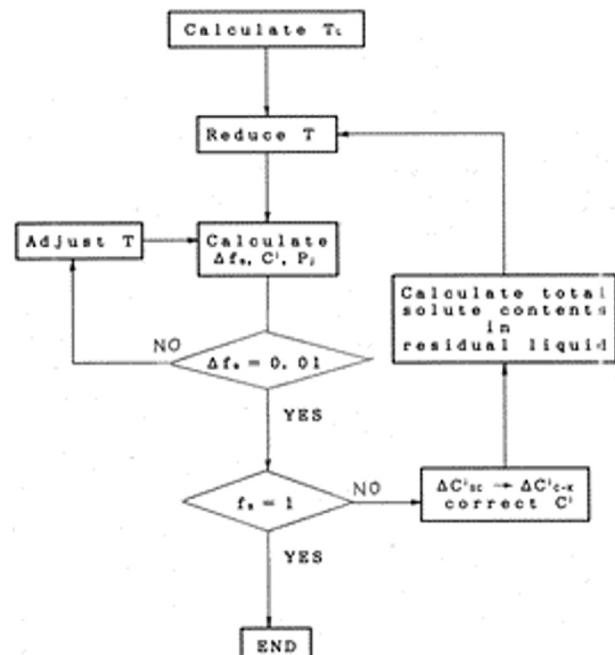


Figure 6. Flow chart of calculation.

concentrations is reduced and adjusted again so that the solid fraction increment is the predetermined value. This cycle is repeated until the solid fraction reaches 1. At this point, amounts and chemical compositions change of nonmetallic inclusions during the solidification of steel can be analyzed.

3.2 Sulfide Shape Control in Anti-HIC Steel [5]

When manganese sulfides precipitate in spot like segregation, a kind of macrosegregation, along the center-line in the continuously-cast slabs of anti-HIC (hydrogen induced cracking) steel they become film like shape after hot rolling and exist in the thickness center in the thick plates, which acts as initiation sites of hydrogen induced cracking in the line pipes made by the plates. As a counter measure, calcium (Ca) is added to the steel in order to change sulfides from MnS to CaS (calcium sulfide). However, MnS precipitation occurs under some conditions even if Ca is properly added. In order to clarify the conditions, the coupled precipitation model is firstly applied.

Spot-like segregation is considered to be formed by solute-enriched residual liquid squeezed out from inter-dendritic region by thermal and solidification shrinkage and slab bulging and trapped in spot-like shape along the centerline of continuously-cast slabs. Based on the measured solute concentrations in spot-like segregation, the residual liquid among dendrites is squeezed out when the solid fraction of dendrite reaches about 0.9 and forms spot-like segregation. The chemical compositions of anti-HIC steel on average and in the residual liquid of growing dendrite at fraction solid of 0.9 are listed in Table I. The latter was calculated by Clyne-Kurz's equation.

Solidification of a spot-like segregation with the diameter of $100\mu\text{m}$ with chemical compositions listed in the bottom row in Table I was analyzed by the coupled precipitation model. Figure 7 shows the calculated soluble solute concentrations (a) and nonmetallic inclusion concentrations (b) as functions of fraction solid. At the start of solidification, almost all oxygen (O) is trapped as $\text{CaO-Al}_2\text{O}_3$ (calcium aluminates) and Ca is firstly used for capturing O and the rest of Ca is used for capturing S (sulfur) as CaS. The results: soluble O is less than

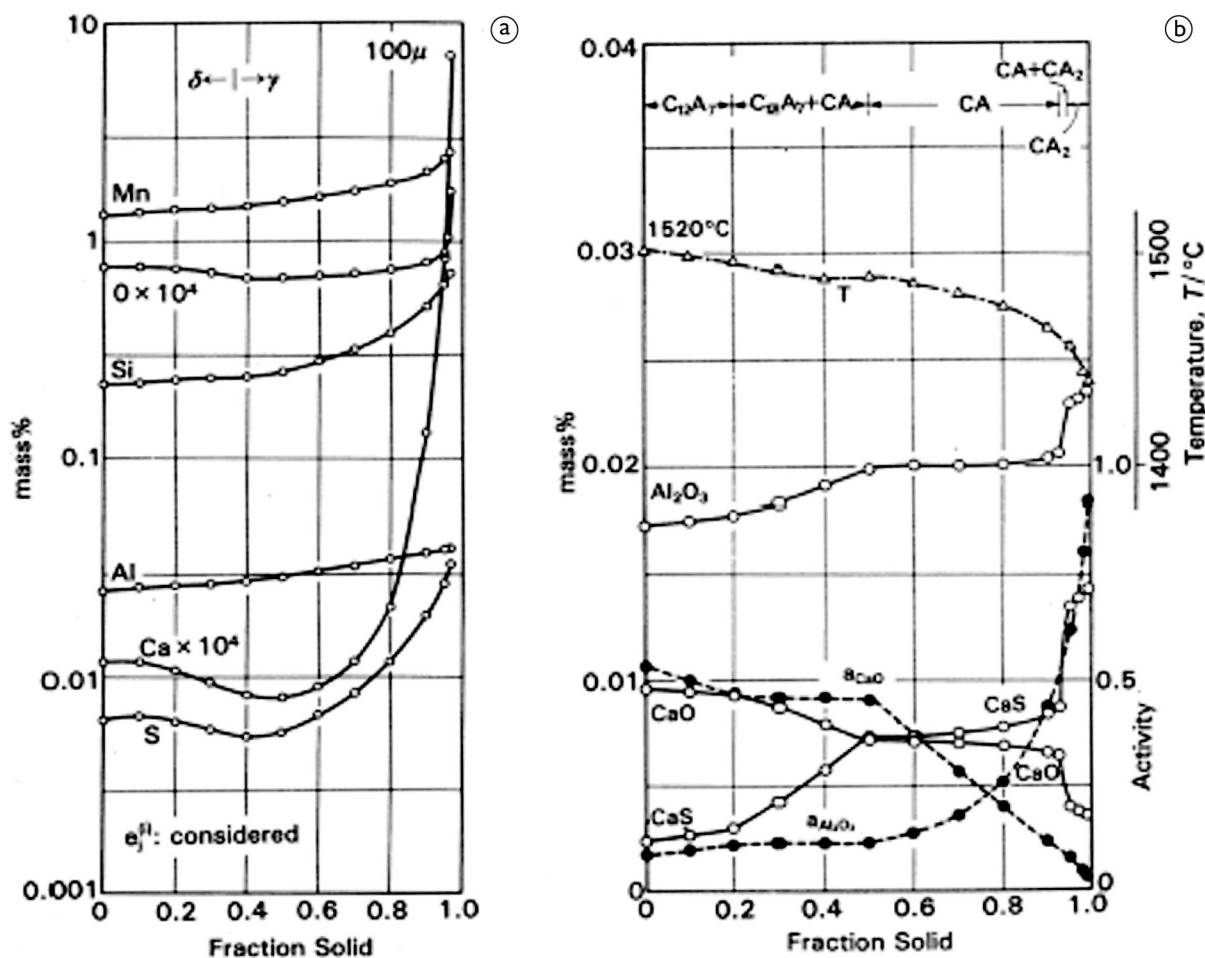


Figure 7. Calculated changes of the amount of dissolved solutes (a) and nonmetallic inclusions (b) in the residual liquid during solidification of a spot-like segregation with the diameter of 100μ .

Table 1. Chemical compositions of anti-HIC steel on average and in the residual liquid of growing dendrite at fraction solid of 0.9 (calculated values) [5]. The latter was calculated by Clyen-Kurz equation with arm spacing of 200 μm .

(%)	C	Si	Mn	P	S	Al	Ca	O
Average	0.081	0.16	1.02	0.0050	0.0012	0.0290	0.0033	0.0025
C_L^{90}	0.317	0.218	1.32	0.0203	0.0090	0.0447	0.0270	0.0270

1 ppm and soluble Ca is around 0.01 ppm. Soluble aluminum (Al) is about 200 ppm and soluble sulfur is about 70 ppm. As solidification proceeds, segregating S decomposes CaO in CaO- Al_2O_3 forming CaS. O from decomposed CaO is captured by soluble Al forming Al_2O_3 . The results, The mass quantity of CaS and the Al_2O_3 ratio in CaO- Al_2O_3 increase as the total solid fraction increases. However, in this case CaO in CaO- Al_2O_3 does not decompose completely and captures segregating S to form CaS throughout the solidification. MnS does not precipitate, that is, sulfide shape control is successful in this case.

On the other hand when the solidification of a spot-like segregation with a diameter of 1000 μm with same chemical compositions is analyzed, precipitation of MnS cannot be prevented (Figure 8). Changes of soluble solute concentrations during the solidification are almost the same as shown before, Figure 7a and general tendency of nonmetallic composition changes are also similar to Figure 7b. However, CaO in CaO- Al_2O_3 is consumed completely at the end of solidification of the spot-like segregation of this diameter as shown in Figure 8. After that there is no Ca source which captures segregating S as CaS. As the result MnS precipitates at the very end of solidification. Since the diffusion distance increases due to the increase of the diameter of the spot-like segregation, the effect of bulk diffusion of S is reduced and enrichment of S in the residual liquid is accelerated, which increases the CaO consumption rate in CaO- Al_2O_3 . As the result CaO is consumed completely before the solidification is completed.

Solidifications of spot-like segregation with various diameters were analyzed and it was found that MnS precipitates in a spot-like segregation at fraction liquid of about 0.01 when its diameter exceeds 300 μm as shown in Figure 9. This threshold diameter for MnS precipitation is in good agreement with the observations. As conclusions in order to succeed in sulfide shape control, size of spot-like segregation is regulated by minimization of slab bulging and by soft reduction of slab thickness at the crater end of continuous casting which just compensates thermal and solidification shrinkage in order to suppress the residual liquid squeezing out of dendrites.

3.3 Control of Oxide Inclusions in an Austenitic Stainless Steel for Wire [6]

Chemical compositions of an austenitic stainless steel for wire is listed in Table 2. When oxides inclusions are not

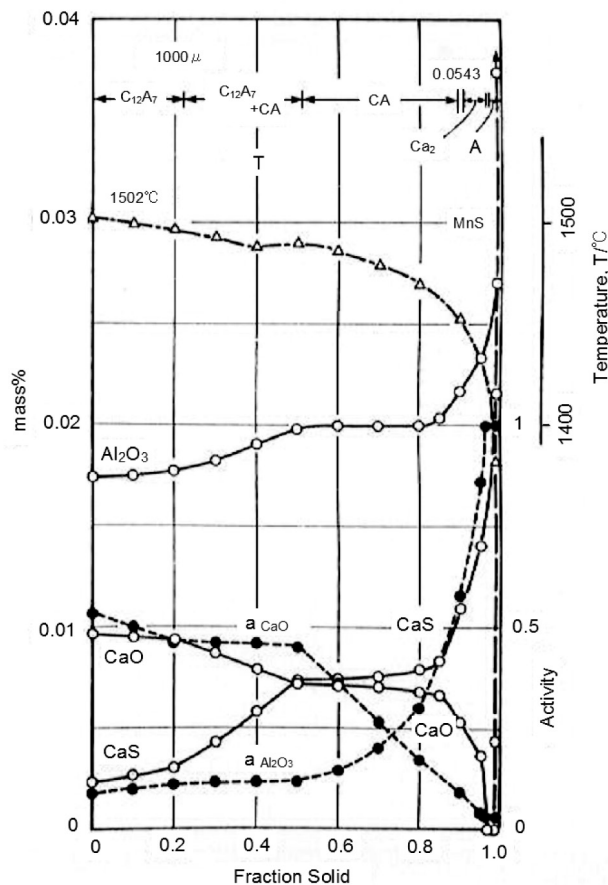


Figure 8. Calculated change of the amount of nonmetallic inclusions in the residual liquid during solidification of a spot-like segregation with the diameter of 1000 μm .

deformed during the hot rolling of this steel, large inclusions are left in the hot-rolled bar, which causes breaking of wire during the succeeding cold wiredrawing process. Therefore, oxide inclusions in the steel should be well deformable at hot rolling temperature. Chemical compositions of oxide inclusions in this steel are analyzed by the coupled precipitation model. Figure 10 shows the calculated Al_2O_3 (alumina) and SiO_2 (silica) contents in oxide inclusions as functions of total O content. The calculated values at fraction solid of 0.5 are in good agreements with observed ones.

The point is that as total O content increases from 40 ppm to 80 ppm Al_2O_3 concentration decreases and SiO_2 concentration increases sharply, which means that the nature of oxide inclusions changes drastically. However, further increase of total O content over 80 ppm does not change

Al₂O₃ and SiO₂ concentrations so much. Both changes are saturated. Therefore, further increase of total O content over 80 ppm just increases the amounts of oxides inclusions, which is not a good idea.

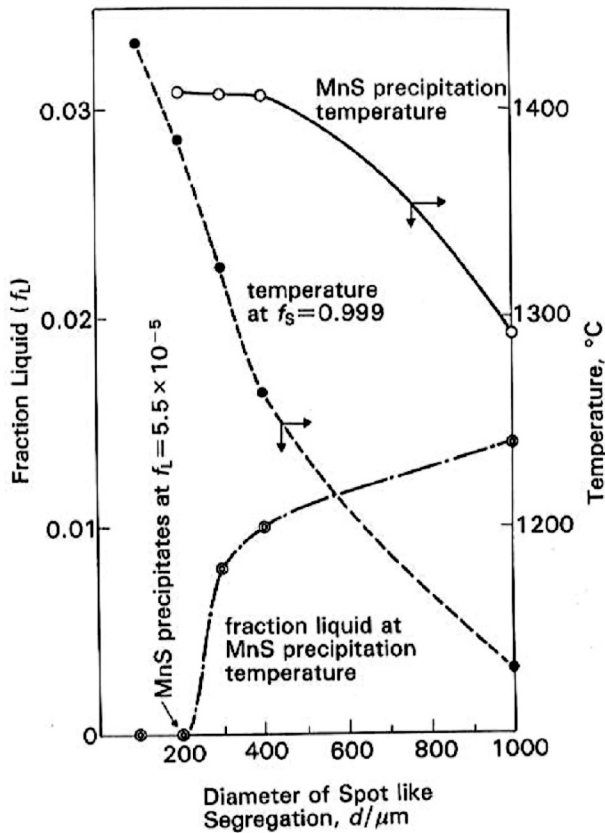


Figure 9. Fraction liquid and temperature when MnS precipitation starts and temperature at fraction solid of 0.999 during solidification of spot-like segregation with various diameters (calculated results) [5].

The amounts of every phase existing in the oxide inclusions in the austenitic stainless steel with total O contents of 40 and 80 ppm calculated at various temperatures are compared in Figure 11. The oxide inclusions in the steel with total O content of 40 ppm are hard crystalline phases such as Al₂O₃ and MgO+Al₂O₃ (spinel), which occupies 40%, even at the high temperature of 1600°C. These inclusions are not considered deformable during hot rolling. On the other hand, in the oxide inclusion in the steel with total O contents of 80 ppm, even at low temperature such as 1200°C, liquid phase occupies 80%. These inclusions are considered deformable during hot rolling. Based on these findings an austenitic stainless steel for wire was successfully developed.

4 CONTROL OF SLAG-METAL REACTION

4.1 Optimization of Manganese Removal Process

In order to realize micro-alloying, alloying element such as manganese (Mn) must be removed almost completely at the beginning of the steel refining. In the manganese removal process, iron oxide (FeO) is injected as flux into hot metal through an immersed nozzle in a transfer ladle. This flux, nearly 100%FeO as injected, oxidizes Mn and Si in hot metal as it floats up to the top slag, after it is injected. Kitamura et al. [7] analyzed the reaction between flux and

Table 2. Chemical compositions of an austenitic stainless steel for wire [6]

Cr	Ni	C	Si	Mn
18.3	10.35	0.02	0.5	1.1
Al	O	Mo	Ca	Mg
0.0015-0.0030	0.0040-0.0150	0.01	0.005	0.0004

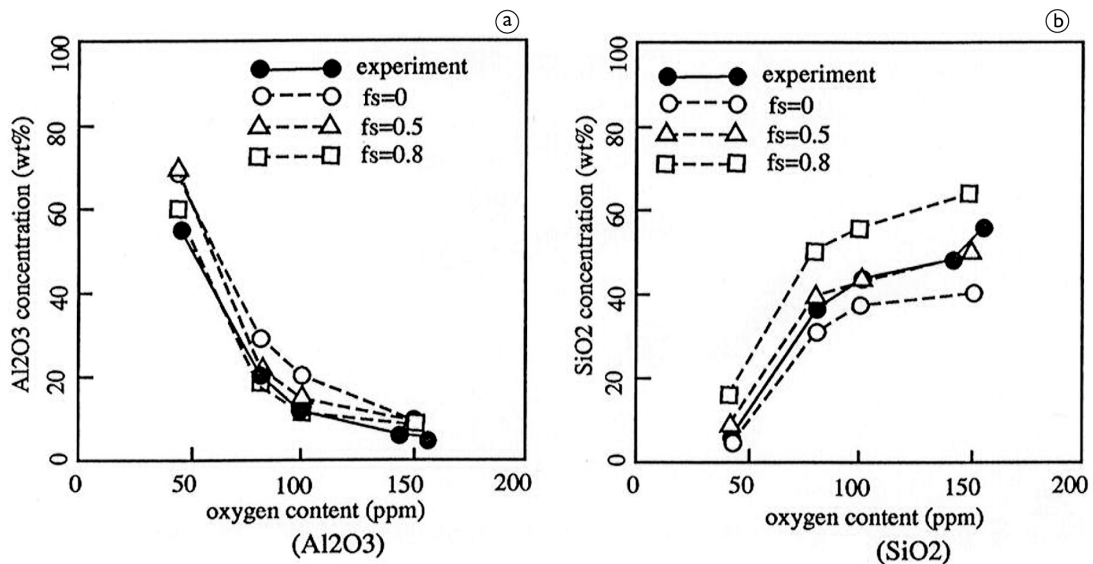


Figure 10. Alumina and silica concentrations in oxide inclusions in an austenitic stainless steel with various total oxygen contents [6].

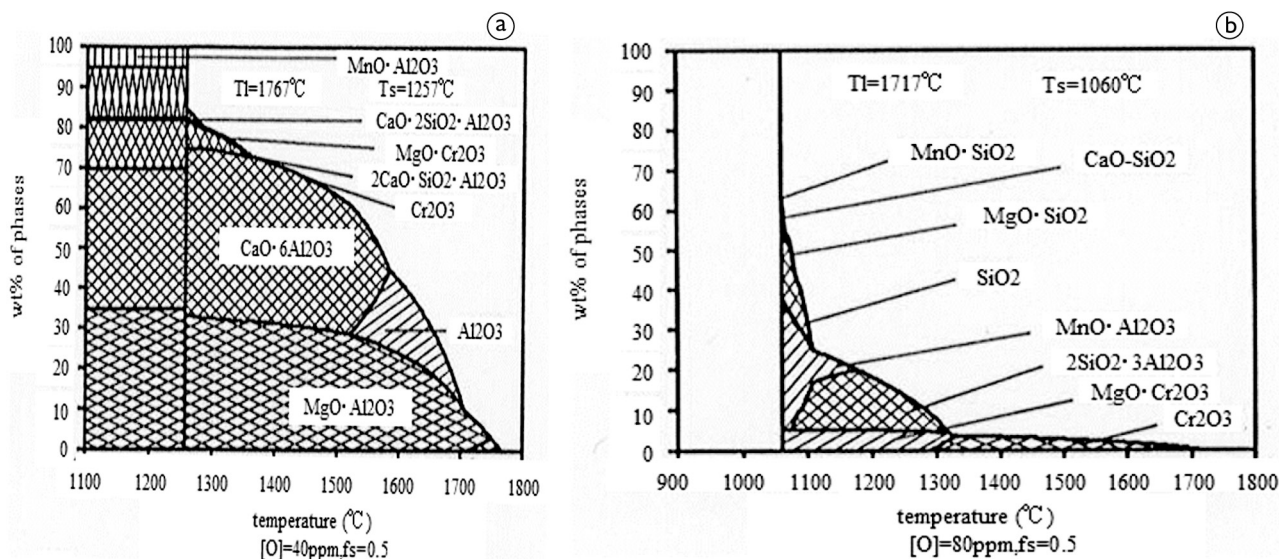


Figure 11. Calculated fractions of various phases at various temperature in oxide inclusions in austenitic stainless steel with total oxygen contents of 40 and 80 ppm [6].

hot metal by the use of coupled reaction model developed by Robertson et al. [8]. In the coupled reaction model, local thermodynamic equilibrium at slag-metal interface, complete mixing both in bulk slag and bulk metal are assumed and diffusion boundary layers are considered both in slag side and metal side along the interface. Reaction rate is assumed to be controlled by the diffusion of solute elements and diffusion of component oxides through each boundary layer.

The calculated FeO, SiO₂ and MnO concentrations in the flux as a function of time after injection in the hot metal are shown in Figure 12. FeO concentration decreases and SiO₂ concentration increases monotonically as the time elapses, whereas MnO concentration increases at the beginning but decreases after it reaches its maximum where oxygen potential is not large enough to oxidize Mn in hot metal and MnO in flux is reduced back to hot metal. From the viewpoint of Mn removal efficiency, it is preferable that the flux reaches top slag and is absorbed by it when Mn concentration reaches the maximum. As the operation of Mn removal process proceeds Mn and Si contents are lowered. As the results, FeO reduction rate in the flux is reduced as the operation proceeds and the time when the MnO content reaches its maximum also becomes longer. This analysis concludes that the depth of immersed nozzle should be increased so that the time for the injected flux needed to float up to top slag is the same as the time required for the MnO content to become its maximum for the optimization of the process.

4.2 Composition Design of Mold Flux in Continuous Casting

The chemical compositions of mold flux changes through the reaction with liquid steel during continuous

casting. In some cases, during the casting of titanium bearing steel, dendritic solid phase CaTiO₃ precipitates in the mold flux due to its chemical composition change, which causes sticking of the initial solid phase to the mold and causes break out in the worst cases. In order to prevent this chemical composition of mold powder is designed with consideration of the reaction with liquid metal during the casting. Kiyose et al. [9] analyzed chemical composition changes of mold flux during the casting of Ti bearing steel by applying coupled reaction model to the flux and metal reaction. In this case fresh mold flux is supplied to bulk flux from the top, reacted flux is removed from bulk flux through the gap between mold surface and initial solid shell, fresh liquid steel is supplied to bulk metal through immersion nozzle and reacted metal is removed from the bulk metal through mold exit. These in-flows and out-flows are also included in addition to diffusion controlled reaction between the flux and the metal to update the chemical compositions of mold flux and liquid metal in the mold.

The chemical compositions of steel and mold fluxes used in the analysis are listed in Tables 3 and 4, respectively. Flux A has higher basicity than flux B. Figure 13 shows the calculated chemical composition change during the casting. As casting time elapses, SiO₂ concentration decreases and TiO₂ concentration increases due to the oxidation of Ti in liquid metal by SiO₂ in the flux. The increment of TiO₂ concentration and the decrement of SiO₂ concentration are larger in the case of flux A than flux B. The trajectories of calculated flux composition change are shown on SiO₂-CaO-TiO₂ pseudo ternary diagram in Figure 14, where equi-activity curves of TiO₂ are also drawn. In the region with basicity lower than 0.5, TiO₂ activity increases rapidly as TiO₂ concentration increases, which discourages oxidation of Ti in liquid metal. As a result TiO₂ concentration does not increase so much

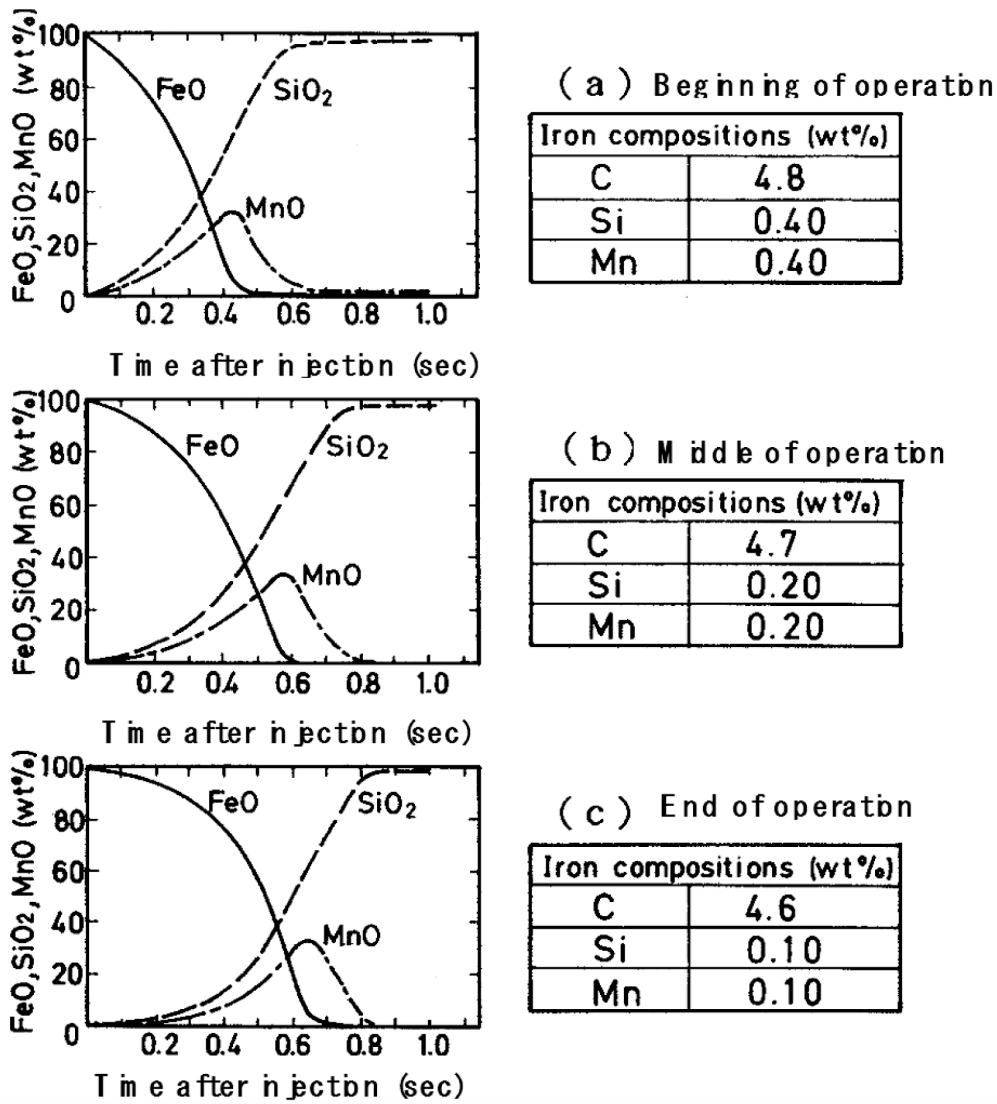


Figure 12. Changes of FeO, SiO₂ and MnO concentrations in flux after it is injected into hot metal at beginning, middle and end of operation of Mn removal [7].

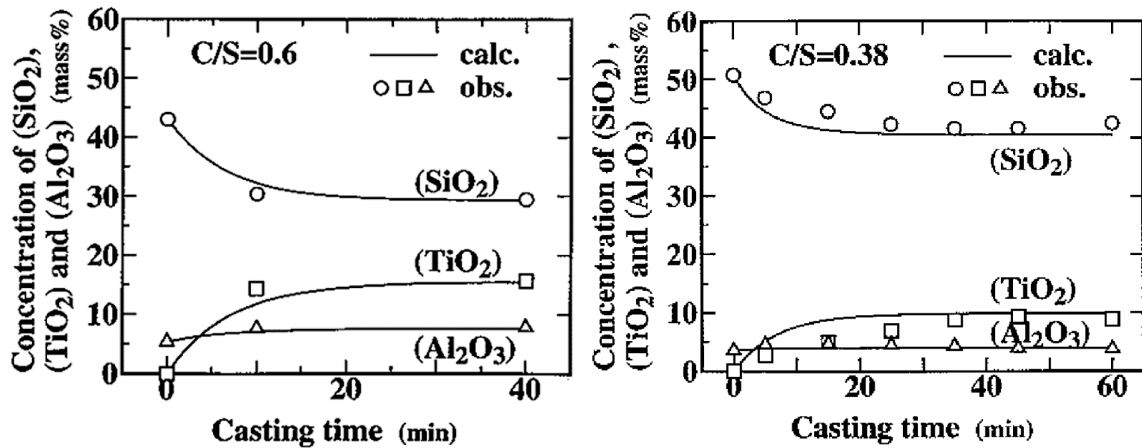


Figure 13. Calculated changes of SiO₂, TiO₂ and Al₂O₃ contents in Flux A (on the left) and Flux B (on the right) during casting of the Ti-bearing steel [9].

and even in the terminal chemical composition CaTiO_3 does not precipitate in the case of flux B. On the other hand in the region with basicity higher than 0.5, TiO_2 activity does not increase so much as TiO_2 concentration increases, which encourages oxidation of Ti in liquid steel by SiO_2 in flux. So TiO_2 concentration increases and CaTiO_3 precipitates in the case of flux A. By the use of this kind of analysis mold flux are designed according to the steel to cast.

5 PROCESS CONDITION DESIGN FOR STEEL PROPERTIES

5.1 Quenching Conditions for Fatigue Crack Arresting in Thick Plates [10]

As shown in Figure 15, the amount of gamma (austenite) phase decreases due to gamma to alpha transformation in 0.12%C-steel as temperature goes down from 850 °C, whereas carbon content in gamma phase increases, although this is not shown. By quenching the steel at some temperature during this cooling, residual gamma phase at this temperature is transformed to martensite.

The hardness of the martensite increases with its carbon content as shown in Figure 16. By the combination of these figures the amount and hardness of martensite obtained by quenching 0.12%-steel can be shown as functions of the quenching temperature as in Figure 17, where the volume fraction of austenite is equivalent to that of martensite. For fatigue crack arresting in this steel a fraction of martensite over 0.2 with Vickers hardness of over 500 is required. In order to satisfy this requirement it is concluded that the quenching should be done below 750°C and above 700°C.

5.2 Heat Treatment Design for Toughness, Fatigue Strength, etc. In Steels for Gear, Spring and Valves [12]

In order to increase the toughness and fatigue strength and to suppress undesired deformation of gears, springs and valves, grain growth is suppressed by the dense dispersion of fine carbides and nitrides throughout their production process. In order to obtain this dense dispersion of fine precipitates, large carbides and nitrides in the steel should be dissolved once completely during solution treatment at the beginning. On the other hand, grains grow excessively when the heating temperature of solution treatment is unnecessarily high. Figure 18 shows the amounts of AlN (aluminum nitride) and Nb(CN) (niobium carbonitride) estimated by thermodynamic equilibrium calculation at various heating temperature, which approximately agree with experimental observations (Figure 19). This demonstrates that by the use of estimation by thermodynamic equilibrium calculation the solution treatment temperature can be chosen as around 1200 °C for this steel.

Table 3. Chemical compositions of steel (mass%)

C	Si	Mn	Al	Ti	O
0.03	0.34	0.34	0.044	0.33	0.015

Table 4. Chemical compositions of mold fluxes (mass%)

	CaO	SiO ₂	Al ₂ O ₃	Na ₂ O	CaF ₂
A	26	43	5	12	14
B	19	51	3	13	13

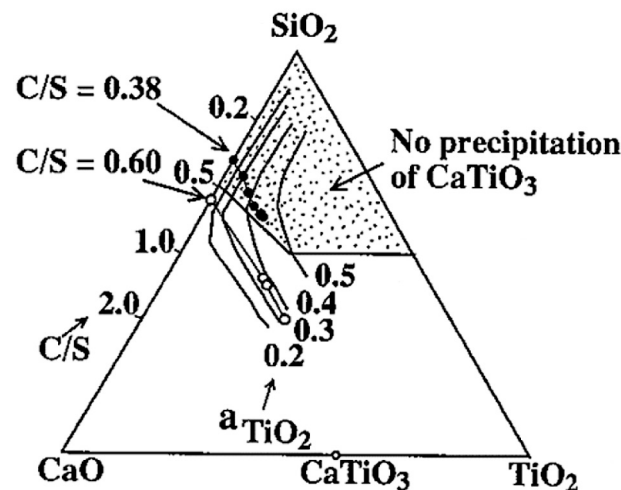


Figure 14. Calculated chemical composition change of flux A and B during casting of Ti-bearing steel [9].

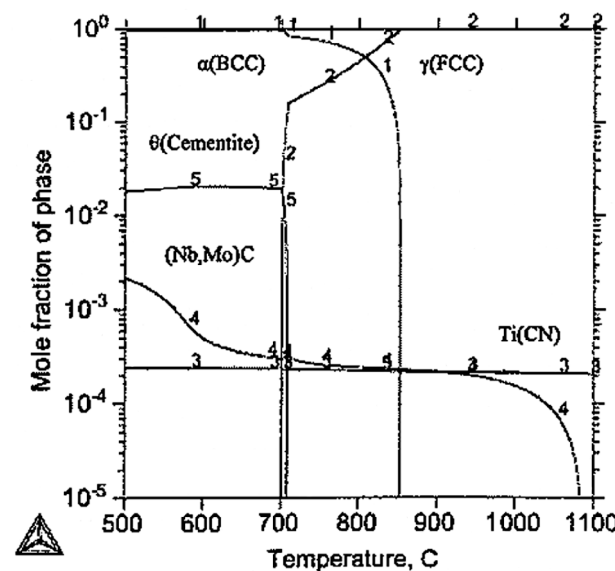


Figure 15. Stable equilibrium phase diagram as a function of temperature in 0.12%C-steel [10].

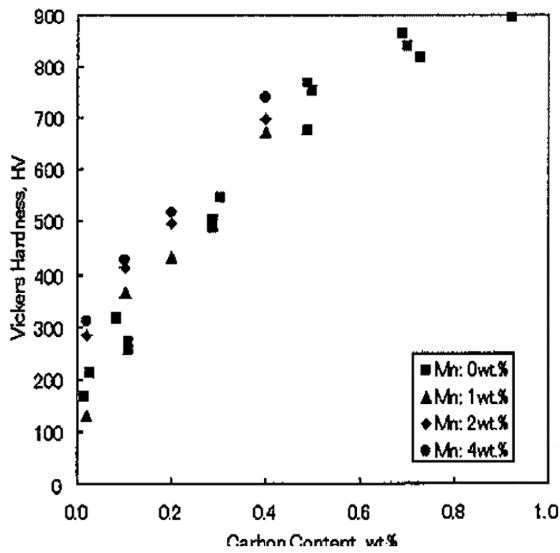


Figure 16. Hardness of martensite with various C and Mn [11].

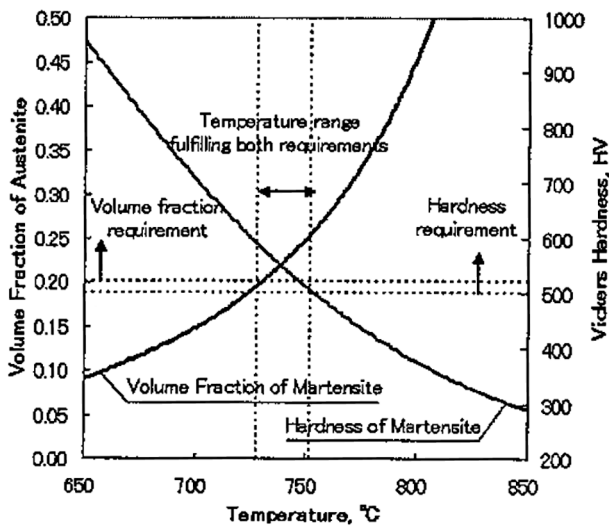


Figure 17. Volume fraction of austenite at various temperature and hardness of martensite obtained by quenching the austenite [10].

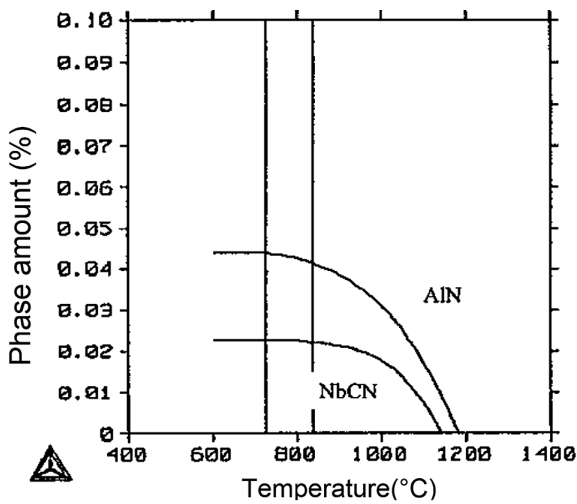


Figure 18. Calculated dissolution behavior of AlN and Nb(CN) [12].

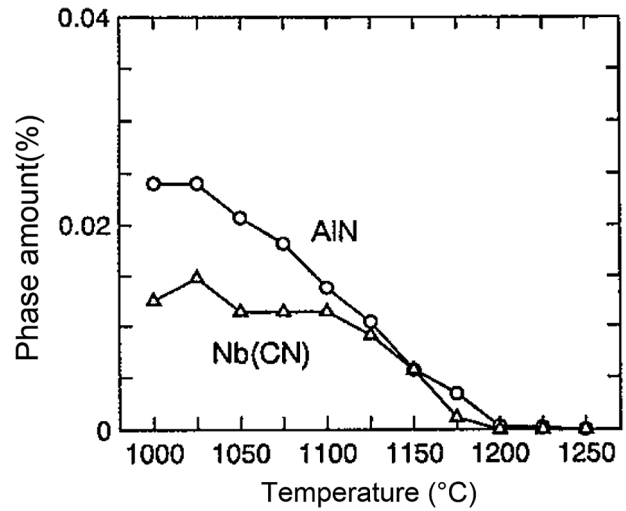


Figure 19. Observed dissolution behavior of AlN and Nb(CN) [12].

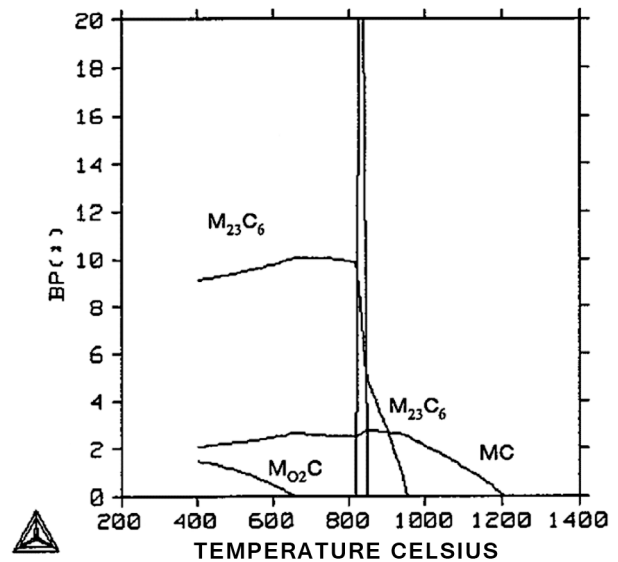


Figure 20. Calculated precipitation behavior of various carbides in bearing steel [12].

In order to improve anti-erosion property of bearing steel, appropriate distribution of carbides is necessary. This is also realized by estimating the types and amounts of carbides formed, by the use of thermodynamic equilibrium calculation as shown in Figure 20.

4 CONCLUSIONS

Using several industrial examples it was demonstrated how computational thermodynamics and phase diagrams can be useful in the understanding and solving problems in steel processing.

REFERENCES

- 1 Yamada W, Matsumiya T, Sundman B. Development of a simulator of solidification path and formation of nonmetallic inclusions during solidification of stainless steels. In: Kihara J, Yamamoto R, Doyama M, Suzuki T, editors. Computer aided innovation of new materials. Amsterdam: Elsevier B.V.; 1991. p. 587-590.
- 2 Clyne TW, Kurz W. Solute redistribution during solidification with rapid solid state diffusion. Metallurgical Transactions A, Physical Metallurgy and Materials Science. 1981;12A(6):965-971. <http://dx.doi.org/10.1007/BF02643477>.
- 3 Scheil E. Bemerkungen zur Schichtkristallbildung. Zeitschrift fur Metallkunde. 1942;34:70.
- 4 Koseki T, Matsumiya T, Yamada W, Ogawa T. Numerical modeling of solidification and subsequent transformation of Fe-Cr-Ni alloys. Metallurgical Transactions A, Physical Metallurgy and Materials Science. 1994;25A(6):1309-1321. <http://dx.doi.org/10.1007/BF02652305>.
- 5 Matsumiya T. Mathematical analyses of segregations and chemical compositional changes of nonmetallic inclusions during solidification of steels. Materials Transactions JIM. 1992;33(9):783-794. <http://dx.doi.org/10.2320/matertrans1989.33.783>.
- 6 Yamada W, Matsumiya T, Fukumoto S, Tanaka S, Takeuchi H. Simulation of the compositions of nonmetallic inclusions in cast stainless steels. In: Proceedings of the International Conference on Computer-assisted Materials Design and Process Simulation; 1993 Sept. 06-09; Tokyo, Japan. Tokyo: The Iron and Steel Institute of Japan; 1993. p. 123.
- 7 Kitamura T, Shibata K, Sawada I, Kitamura S. Technology development by computer simulation for refining process optimization. Bulletin of JIM. 1989;28:310. Japanese.
- 8 Robertson DGC, Deo B, Oguchi S. A multicomponent mixed transport control theory for the kinetics of coupled slag-metal and slag-metal-gas reactions: application to desulphurization of molten iron. Ironmaking & Steelmaking. 1984;11:41.
- 9 Kiyose A, Miyazawa K, Yamada W, Watanabe K, Takahashi H. Mathematical modelling of change in composition of mold flux in continuous casting of steels. ISIJ International. 1996;36(Supplement):S155-S158. http://dx.doi.org/10.2355/isijinternational.36.Suppl_S155.
- 10 Mizutani Y. Current progress in development of heavy plate steel based on thermodynamic calculation. Ferrum. 2007;12:291. Japanese.
- 11 Irvin KJ, Pickering FB, Garston J. The effect of composition on the structure and properties of martensite. Journal of the Iron and Steel Institute. 1960;196:66.
- 12 Ochi T. Current progress in application of calculated phase diagram to development of bar and wire rod. Ferrum. 2007;12:363. Japanese.

Received: 1 Dez. 2015

Accepted: 14 Dez. 2015